Cross-shore migration of lunate megaripples during Duck94

Amani S. Ngusaru[1]

Department of Earth Sciences, Memorial University of Newfoundland, St. John's, Newfoundland, Canada

Alex E. Hay

Department of Oceanography, Dalhousie University, Halifax, Nova Scotia, Canada

[1] Remote acoustic observations of lunate megaripple migration are presented from two storm events during the Duck94 nearshore dynamics experiment for time periods during which longshore currents were weak (<20 cm/s). During these periods, significant wave orbital velocities were 50–80 cm/s; megaripple heights were 0.05–0.5 m; megaripple horns were directed shoreward; the crest-to-trough slope of the shoreward advancing ripple face was close to the angle of repose; and migration speeds were 10–40 cm/h onshore. The observations also indicate that the megaripples stalled, and may have begun to migrate offshore, when the mean offshore flow exceeded 20 cm/s during the second storm. Stress-based bed load sediment transport models are moderately successful in predicting the observed dependence of migration velocity on measured fluid velocities separated into zero (mean current), infragravity wave, and sea-and-swell wave frequency bands. Wave and mean current friction factors, f_w and f_c, are obtained by best fit between the predicted and observed migration velocities, for two choices (3/2 and 5/2) for the stress exponent ξ in the bed load transport part of the model. Net transport is computed using wave velocity amplitudes determined from both run length statistics and wave by wave. Improved agreement with observations is obtained for the wave-by-wave net transport predictions and for the wave-like treatment of the infragravity band. The level of agreement is relatively insensitive to the value of ξ. The best fit current and wave friction factor values, for $\xi = 5/2$ and 3/2 are $f_c = 4.3 \times 10^{-3}$ and 8.0×10^{-3} and $f_w = 1.7 \times 10^{-2}$ and 4.8×10^{-2}, respectively. _INDEX TERMS:_ 4546 Oceanography: Physical: Nearshore processes; 4558 Oceanography: Physical: Sediment transport; 3022 Marine Geology and Geophysics: Marine sediments—processes and transport; _KEYWORDS:_ megaripples, bedforms, bedload transport, sediment dynamics, nearshore hydrodynamics

1. Introduction

[2] The sedimentary bed forms occurring in marine environments have been a subject of many geological, oceanographic and engineering studies. A number of these studies have suggested the potential of bed form migration as a measure of bed load transport; for example, _Boyd et al._ [1988]. However, the complex relationship among bed forms, sediment transport, and nearshore hydrodynamics is still poorly understood, especially for cases involving the combined effects of waves and currents.

[3] Progress toward a better understanding of bed forms in the nearshore zone was constrained historically by the lack of suitable methods for observing bed form development in highly active transport conditions. Early measurement methods were based on photographic or video techniques [e.g., _Kachel and Sternberg_, 1971; _Boyd et al._, 1988; _Wright et al._, 1991]. However, optical methods are less useful during storms because visibility is degraded by sediment in suspension (although the useful range of optics can be extended through the addition of structured lighting [_Crawford and Hay_, 1998]). In recent years, high-frequency acoustic techniques have been developed for bed form measurement and are leading to considerably improved knowledge of mobile bed evolution during intense forcing. These developments began with the introduction by _Dingler_ [1974] [see also _Dingler et al._, 1977] of an acoustic altimeter on a mechanically driven horizontal track. Acoustic altimeters have since been used in stationary mode to estimate bed form profiles during migration past a fixed point, either singly or in an array, the latter providing migration velocity in addition to the bed form profile [_Hay and Bowen_, 1993; _Gallagher et al._, 1998; _Traykovski et al._, 1999]. _Hay and Wilson_ [1994] introduced rotary side scan sonars to obtain 2-D plan view images of the bed form field during storm events in the nearshore zone. This

---

[1]Now at Institute of Marine Sciences, University of Dar es Salaam, Zanzibar, Tanzania.
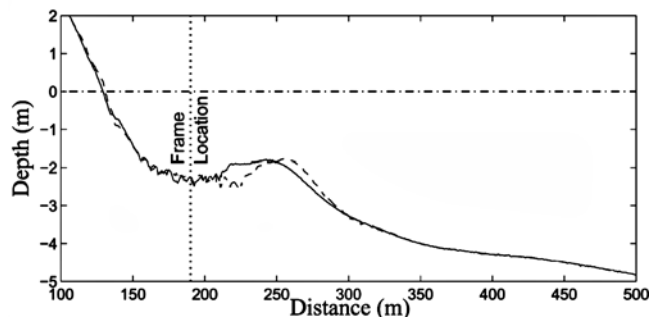
Figure 1. Cross-shore bathymetric profiles for year day 277 (solid) and 285 (dashed) along a line about 10 m north of the instrument frame. The frame location (vertical dotted line) was near the center of the trough at 190 m in the cross-shore coordinate, about 60 m from the shoreline. Note the O(10 cm) bed elevation variations in the trough: these are due to megaripples.

approach has also proved to be useful for observing bed form evolution on the continental shelf [*Traykovski et al.*, 1999]. The results presented here are based on 2-D imagery obtained with a similar rotary fan beam sonar, augmented by bed elevation profiles obtained with a rotary pencil beam sonar.

[4] Lunate megaripples are comparatively large bed forms characterized by a deep trough which in plan view is crescentic. Following the descriptive terminology of *Allen* [1968], lunate megaripple sizes are known from SCUBA observations [*Clifton et al.*, 1971] to range from 0.3–1.0 m in height, and 1–4 m in span (the distance between horn tips). Other lunate megaripple observations in the nearshore zone have been reported [e.g., *Clifton et al.*, 1971; *Dingler*, 1974; *Davidson-Arnott and Greenwood*, 1976; *Hay and Bowen*, 1993; *Hay and Wilson*, 1994; *Gallagher et al.*, 1998]. Because of their large size compared to other sand bed forms, lunate megaripples are major bottom roughness features in the nearshore environment.

[5] The present paper has two main purposes. One is to present our observations of megaripple migration during periods of relatively weak longshore currents when migration was in the cross-shore direction. The second is to compare the observed migration speeds to those predicted using stress-based bed load transport models, in particular the traditional *Meyer-Peter and Müller* [1948] model, developed originally for unidirectional flow, and that proposed more recently for combined wave-current flows by *Sleath* [1995]. A fundamental issue in the application of stress-based models to sediment transport is the appropriate choice of bottom drag coefficient. In combined wave-current flows, the drag coefficients for the mean current and the waves are expected to be quite different both from each other and, for the mean current at least, much different from the values in the absence of wave motion [*Grant and Madsen*, 1986; *Fredsoe and Deigaard*, 1992; *Nielsen*, 1992]. However, in part because of the difficulties associated with making direct measurements of both the wave and current stresses over mobile beds, there have until quite recently been few empirical constraints on the appropriate choice of wave and current drag coefficients in nearshore environments. In the nearshore zone, there can also be significant energy in the infragravity wave band (i.e.,

frequencies lower than the sea swell band but higher than the tidal and hourly mean longshore current), and the additional question arises as to the appropriate choice of drag coefficient for the fluid motions in this band.

[6] The paper is presented in following order. The experiment, instrumentation, and measurement and analysis methods are briefly described in section 2. The observations are presented in section 3; the ripple migration theory in section 4; and the comparisons between predicted and observed migration velocities in section 5. In section 6, the results are discussed, and the values obtained for the wave and current friction factors from the analysis compared to values expected on the basis of existing semiempirical formulae and other measurements. Section 7 concludes the paper.

2. Methods

[7] The data were collected as part of the Duck94 Nearshore Dynamics Experiment, carried out in October 1994 at the U.S. Army Corps of Engineers Field Research Facility (FRF) in Duck, North Carolina. Incident wave conditions during the experiment were measured by the FRF-operated pressure sensor array in 8 m water depth [see *Birkemeier et al.*, 1985].

[8] Bathymetry was monitored using the FRF's Coastal Research Amphibious Buggy, the CRAB [see *Birkemeier et al.*, 1985]. Figure 1 shows shore normal bathymetric profiles on year days 277 and 285 along a line about 10 m north of the alongshore location of the instrument frame. The bottom profiles are dominated by a nearshore trough and bar system.

[9] The instrument frame (Figure 2) was deployed in the trough inside the primary bar, about 60 m from the shoreline
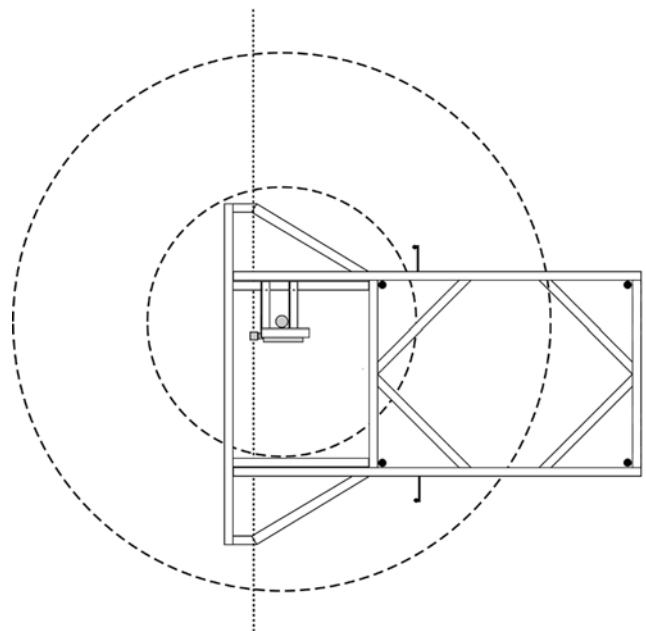

Figure 2. Plan view of the instrument frame, showing pencil beam and fan beam sonars (shaded). The dashed circles are at 1 m radius intervals centered on the fan beam. The dotted line is the intersection of the pencil beam with the seabed. Offshore (east) is toward the top of the figure, and north is to the left.

in 2 m mean water depth. Sensors mounted on the frame included Marsh-McBirney electromagnetic (EM) flow-meters, two Viatran pressure sensors, and 2.25 MHz Simrad-Mesotech rotary acoustic sounders. The EM flowmeters were mounted on both the seaward and landward sides of the frame at 35 and 70 cm nominal heights above bottom. Unless indicated otherwise, the velocity measurements reported here are from the lower seaward flowmeter, for which the data are considered to be the most reliable [*Ngusaru*, 2000]. Velocity, pressure and temperature were sampled at 10 Hz.

[10] The fan beam and pencil beam transducer heads were positioned as shown in Figure 2, at about 1 m height above bottom. This height varied with time depending on bed form migration and larger-scale bed elevation changes during the two storms. Because of the angle of inclination of the fan beam transducer with respect to the horizontal, and the transducer beam pattern, features within the 1 m radius ring were not imaged. The pencil beam transducer rotated about a horizontal axis parallel to the shoreline, providing a shore normal bed profile across the area imaged by the fan beam transducer. The pencil beam transducer was located 22 cm below and 30 cm to the north of the fan beam transducer, and 15 cm closer to shore. The resolution in range and azimuth angle (about the axis of rotation) of the sonar data are determined by a combination of transducer beam width, transmitted pulse length, and signal averaging. The data were acquired at an analog-to-digital conversion rate of 250 kHz at 12-bit resolution. Three consecutive samples were block-averaged, so the range resolution of the stored data was 0.9 cm, comparable to the 0.75 cm two-way travel time length of the 10 μs transmitted pulse. The backscatter profiles from 4 consecutive transmitted pulses were averaged to reduce noise. The transducer head is rotated by a stepper motor, 0.225° per pulse transmission. The angular resolution of the stored data was therefore 0.9°, identical to the nominal angular width of the conical pencil beam, and to the width in azimuth of the fan beam.

[11] The quality of individual rotary scans can be affected intermittently by suspended sediment and bubbles. In order to reduce these contamination effects, 5 successive scans were averaged together. (Each 360° rotation of the transducers required 37 s for the control settings used in this experiment, so 5 successive rotations took 3 min.) This ensemble averaging reinforced the repeatable bottom echo and suppressed random contributions from bubble and suspension plumes. The averaged fan beam images were slant range-corrected using the height above bottom determined from the pencil beam profiles. Five-scan ensemble-averaged images were typically collected at 0.5 hour intervals.

[12] Bed profiles were determined from the 5-scan ensemble-averaged rotary pencil beam images by defining the range corresponding to the maximum backscatter amplitude as the distance to bottom at each angle. Cross-shore migration velocities were determined by cross-correlating bed profiles one hour apart. Prior to cross correlation, the profiles were despiked, interpolated onto a regular grid (0.5 cm spacing), low-pass filtered (second-order Butterworth filter with 5 cpm cutoff frequency), and then resampled at 2.5 cm spacing. Lagged (distance) cross-correlation functions were computed from filtered and detrended bed profile pairs separated by one hour. Migra-

tion velocities were determined from the distance lag corresponding to the central peak in the cross-correlation function. Because of the increase with range in the beam diameter and angle of incidence at the bed, the profiles at distances beyond 2.5 m from the center were noticeably noisier and less well resolved. In addition, because of the high relief of the megaripples relative to the elevation of the sonar head above bottom, parts of the outer edges of the bed profiles (beyond 3.5 m horizontal distance typically) were often in the acoustic shadow of a ripple crest nearer the transducer. Thus only the central section of each profile (typically up to 7 m in length) was used in the cross-correlation analysis.

[13] The fan beam images were slant range-corrected using the height of the sensor above bottom determined from the pencil beam profiles, and then interpolated onto a Cartesian grid at 1.8 cm resolution. Megaripple migration velocities were determined using rectangular subimages from pairs of these 5-scan ensemble-averaged, 1.8 cm pixel square grid fan beam images by 2-D cross-correlation analysis. Each rectangular subimage contained an individual megaripple. In order for these migration velocities to be directly comparable to those estimated from bed profiles, the individual megaripples were selected along the line where the pencil beam intersected the fan beam images. The size of the second subimage in each pair was larger by twice the number of lags used, in both the alongshore and cross-shore directions, to eliminate edge effects. The subimages were also selected from the offshore half of each full fan beam image, because the shoreward facing slip faces provided the highest contrast on the offshore side of the image. The time interval between the subimages in each pair was typically one hour.

[14] The nominal resolution limit for the migration velocities estimated from the pencil beam profiles is 2.5 cm/h, the resolution of the low-pass filtered and resampled bed elevation profiles. This nominal resolution is physically consistent with the width of the pencil beam footprint on the bed at 1 m range, which is 1.6 cm at best (vertical incidence) based on the 0.9° beam width. For the fan beam data, the slant range-corrected and xy-gridded images were constructed of pixels 1.8 cm on a side. Thus the resolution of the fan beam migration velocity estimates due to image resolution alone is also roughly 2 cm/h. (Note that since the cross-shore component of migration is of interest here, and the subimages were taken along the pencil beam line of intersection (Figure 2), it is primarily the (constant, 0.9 cm) resolution in range, not the range-dependent width in azimuth of the acoustic beam resolution, which controls the resolution of the x component of the correlation function.)

3. Observations

3.1. Hydrodynamics

[15] Two storms occurred during the Duck94 experiment: the first, between year days 276 and 279, involved significant wave heights up to 2.5 m at the 8 m array (Figure 3a); the second started on year day 283 producing up to 3.5 m significant wave heights. Peak wave periods, T_p, corresponding to the peak energy spectral density at the 8 m array, were 6.5($\pm$1.2) s during the first storm, and 8.4($\pm$0.9) s during the second storm, the numbers in
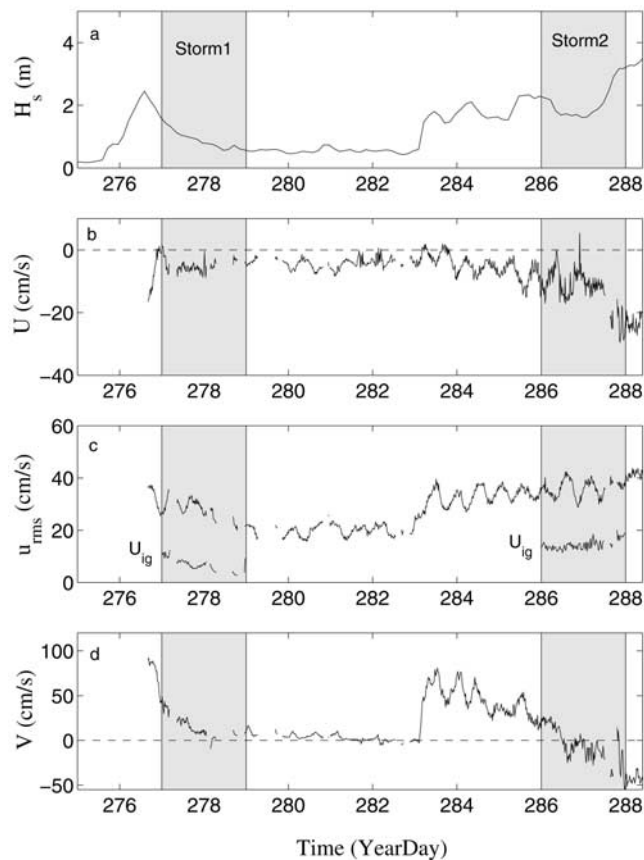
Figure 3. Hydrodynamic conditions at the frame location: (a) significant wave height, H_s, (b) mean cross-shore velocity, U, (c) RMS cross-shore wave orbital velocity, U_{rms}, and (d) mean longshore velocity, V. U is positive onshore; V is positive southward. The shaded areas indicate the intervals during the two storms when cross-shore migrating lunate megaripples were observed. Data in Figure 3a are from the 8 m array; those in Figure 3b–3d are from the lower flowmeter on the seaward side of the instrument frame.

parentheses indicating the range. Figures 3b, 3c, and 3d show the half-hourly average cross-shore current, U, the root mean square cross-shore wave orbital velocity, u_{rms}, and the longshore current, V, respectively, as measured by the lower flowmeter on the seaward side of the frame. The x coordinate and u velocity component are positive on-shore. The longshore coordinate y and velocity component v are then positive southward, since the shorenormal at the FRF is almost east-west.

[16] The fan beam imagery was dominated by cross-shore-oriented lunate megaripples on year days 277–279 during the first storm, and year days 286–288 during the second. These periods, which are indicated by the grey shading in Figure 3, were also characterized by weak (<20 cm/s) longshore currents, except early in the first shaded interval, and late in the second (Figure 3d). For the remainder of this paper, these periods (year days 277–279 and 286–287) will be referred to as the Storm1 and Storm2 intervals.

[17] The cross-shore current (Figure 3b) was mostly directed offshore throughout the duration of the record.

This offshore directed cross-shore current was consistently recorded by all four current meters on the frame [*Ngusaru*, 2000]. The cross-shore current was relatively weak (<10 cm/s) during the Storm1 interval compared to the Storm2 interval, for which tidally modulated offshore flows of up to 15 cm/s amplitude occurred followed by >20 cm/s offshore flow as the wave forcing intensified on the second half of year day 287. As will be shown later, this increase in mean cross-shore current was associated with a distinct change in the cross-shore migration of the megaripples.

[18] Figure 4 shows the average spectra of the cross-shore velocity for the Storm1 and Storm2 intervals. The energy in the infragravity band (frequencies <0.05 Hz) was higher during the Storm2 interval. Infragravity wave velocities (U_{ig}) were extracted by low-pass filtering (cutoff frequency 0.05 Hz) the de-meaned velocity time series. The spectra were computed using 3000 points and a Hanning window with no overlap, and have a resolution of 0.0033 Hz. Figure 3c shows the U_{ig} time series, plotted as the root mean square departure from the half-hourly means. The rms magnitude of U_{ig} was about 20% of U_{rms} during the Storm1 interval, and up to 50% during the Storm2 interval.

3.2. Pencil Beam Bed Elevation Profiles

[19] Figures 5 and 6 show a series of cross-shore bed elevation profiles, obtained with the rotary pencil beam sonar, for the Storm1 and Storm2 intervals respectively. The spikes in some of the profiles were caused by contamination of the bottom signal by sediment plumes.

[20] Qualitatively, the Storm1 interval bed profiles (Figure 5) are dominated by 20–40 cm high megaripples, with pronounced on-offshore asymmetry and 1–2 m trough-to-trough separations, clearly migrating to the right of the figure (i.e., onshore) in the direction faced by the steep crest-to-trough slopes. Thus the on-offshore asymmetry is pitched forward in the direction of migration. Recall that the cross-shore current during the Storm1 interval was directed offshore (Figure 3b), opposite to the direction of ripple migration.
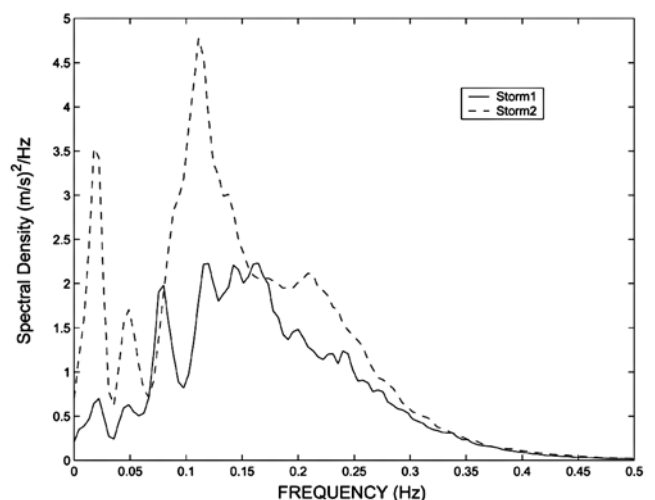

Figure 4. The average cross-shore velocity spectra for the Storm1 and Storm2 intervals. Note the higher energies overall and the higher infragravity energy relative to the incident band during the Storm2 interval.
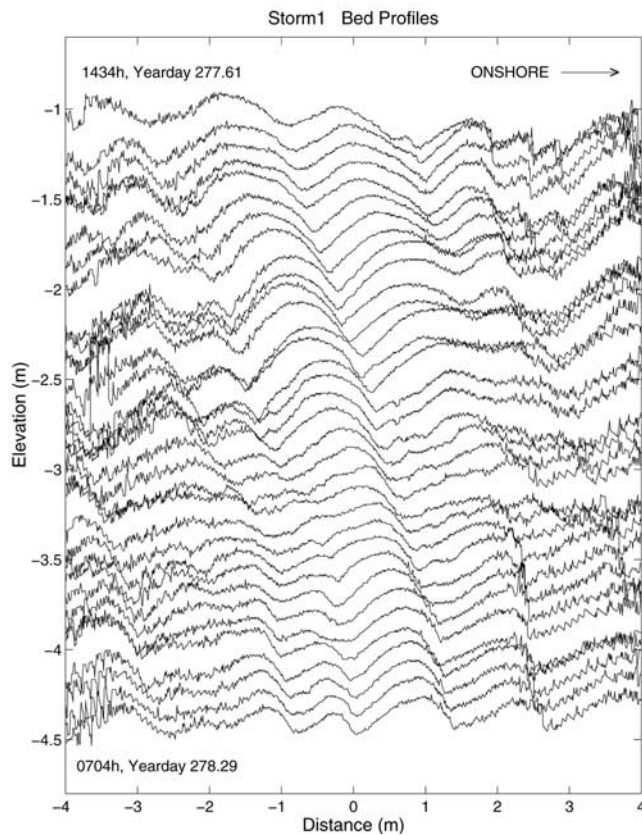
Figure 5. A series of unfiltered pencil beam bed profiles at 1/2 hour intervals during the Storm1 interval. Time increases from top to bottom. The times for the first and last profile are shown. Successive profiles are offset vertically by $-0.2t$ m, where t is the time in hours after the first profile. Note the shoreward migrating bed forms with $15-30$ cm heights, O(1 m) horizontal scale, shoreward asymmetry, and persistence in some cases for the full 0.7 days shown.

[21] Figure 6 shows a series of bed profiles for the Storm2 interval: compared to Figure 5, the megaripples during this period had longer ($2-4$ m) trough-to-trough separations, comparable heights (note the change in vertical scale). Migration was onshore throughout the first three quarters of the 1.6 day interval, again opposite to the cross-shore current which ranged from 5 to 20 cm/s offshore during this period (Figure 3b). Toward the end of the interval, the persistent shoreward migration disappears: this change in apparent migration speed and/or direction coincided with the increased strength of the offshore current.

3.3. Fan Beam Data

[22] Typical fan beam images during the Storm1 interval are shown in Figure 7. Only the offshore halves of the images are presented. The darker shades of grey represent higher backscatter amplitudes. The white and light grey zones are areas of acoustic shadow. To the lower right in each image, dark (acoustically bright) echoes from two frame posts and the lower EM flowmeter and its support are visible, as are their (white) acoustic shadows projected onto the seabed and radiating outward from the center of the image. Lunate megaripples can be identified in these images as concave shoreward bright reflectors. The orientation of

the steep faces of the megaripples and crescentic shapes indicate onshore migration. Small-scale (<25 cm wavelength) ripples are also present. Individual megaripples can be seen to migrate shoreward through the set of images: for example, the feature near coordinate [6, 4'].

[23] Fan beam images from the Storm2 interval also reveal the presence of lunate megaripples (Figure 8). These images correspond to a 2 hour period on day 287 during the first stage of the Storm2 interval. Many of the lunate features migrated shoreward through the full image sequence: for example, the group of megaripples at the top of the images, near grid points [4, 5'] through [8, 5'] initially; and the single lunate megaripple near grid point [7, 3'] initially. In addition, this image sequence shows the rapid development of northward facing lunate forms: for example, near coordinate [5, 4']. The development of the northward facing forms was associated with strengthening of the longshore current during this period (Figure 3d).

3.4. Cross-Shore Migration Velocities

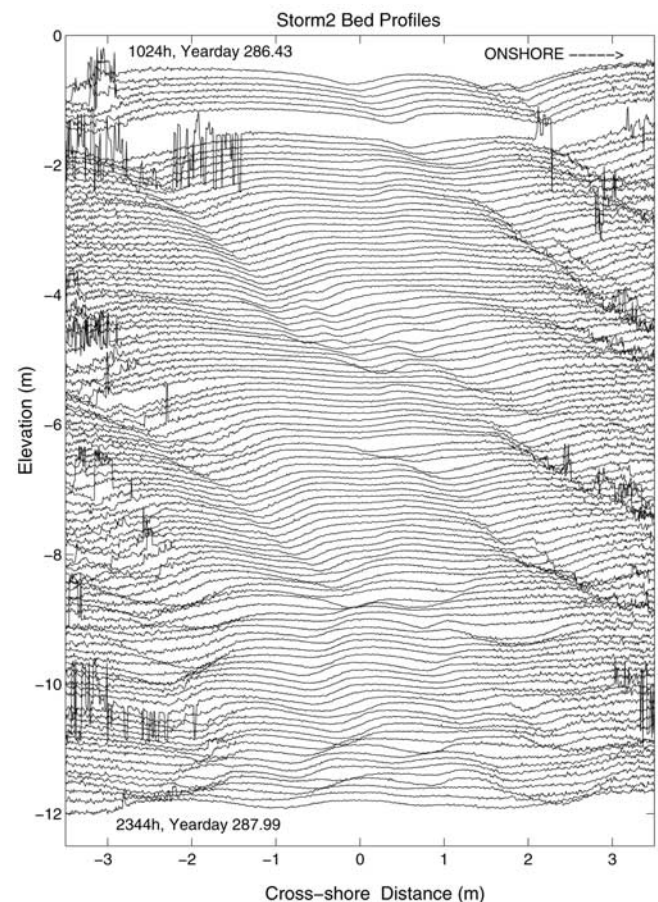[24] The measured cross-shore migration velocities are shown in Figure 9. The results obtained using the two

Figure 6. A series of unfiltered pencil beam bed elevation profiles at 20 min intervals for 1.6 days during the Storm2 interval. Time increases from top to bottom. The times for the first and last profile are shown. Successive profiles are offset vertically by $-0.3t$ m, where t is the time in hours after the first profile. Note the onshore migration early in the interval and the more confused pattern later (i.e., last 25%).
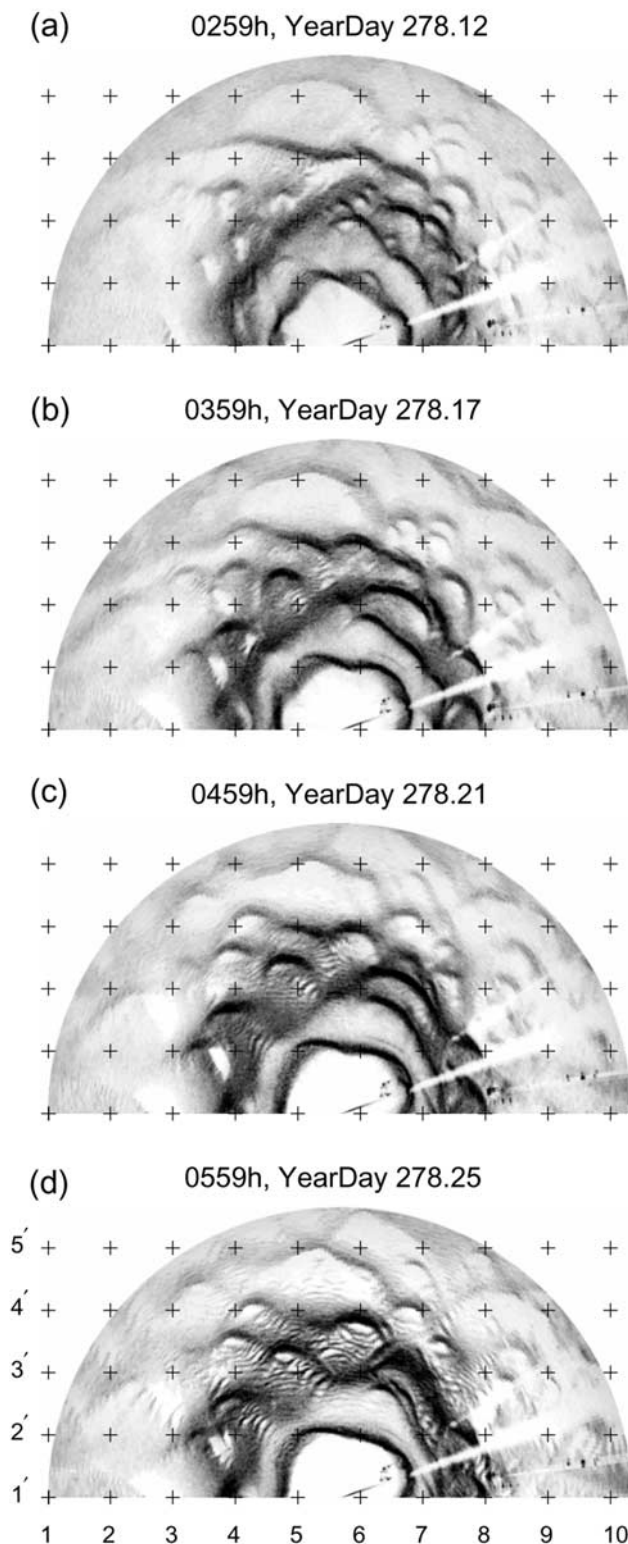
(a) 0259h, YearDay 278.12

(b) 0359h, YearDay 278.17

(c) 0459h, YearDay 278.21

(d) 0559h, YearDay 278.25

Figure 7. Fan beam images of lunate megaripples during the Storm1 interval on the offshore side of the frame. The crosses are spaced 1 m apart. Offshore is toward top of each image. Note the shadows cast by frame in the lower right quadrant. Note also the onshore oriented lunate forms, 0.5– 1 m in horizontal scale. Individual lunate features can be seen to migrate shoreward, near grid point [5, 5′], for example (see also Figure 5).

independent (fan beam and pencil beam) methods are in reasonably good agreement for both periods, and indicate that the megaripples were migrating onshore at 10– 20 cm/h during the Storm1 interval, and onshore at 10– 40 cm/h during the first stage of the Storm2 interval before YD287.5. In the latter part of this interval, cross-shore migration effectively ceased and then, according to these data, trended toward offshore migration. Note as well that there are fewer points for the fan beam than the pencil beam for this interval, especially between YD287.6 and 287.8. This was a period of very active suspension and/or bubble injection, contaminating some of the ensemble fan beam images to the extent that clear images of the seabed were not obtained. The pencil beam data, because of its narrower beam width, were much less affected.

[25] The results for megaripple migration rate with respect to the mean cross-shore flow can be compared with previous measurements in the literature: 132 cm/h [*Osborne and Vincent*, 1992]; 15–24 cm/h [*Hay and Bowen*, 1993]; 90 cm/h [*Vincent and Osborne*, 1993]; 50 cm/h [*Hay and Wilson*, 1994]; and 30 cm/h [*Gallagher et al.*, 1998]. In all of these studies, megaripples were found to migrate onshore, and in several [*Osborne and Vincent*, 1992; *Hay and Bowen*, 1993; *Hay and Wilson*, 1994] opposite to the direction of the mean cross-shore flow. However, the magnitude of the mean cross-shore current was rather small for all of these observations. For example, 5 cm/s by *Osborne and Vincent* [1992] and 2 cm/s by *Hay and Wilson* [1994].

[26] Figure 10a shows the mean cross-shore current plotted against migration velocity from the present data set. The correlation between cross-shore migration velocity and mean cross-shore current is weak (R = 0.16). However, there is a very clear cluster of points in the upper right indicating onshore migration in the presence of offshore flow. In addition, there may be an indication that strong (>15 cm/s) offshore currents are associated with near zero and offshore migration velocities, but the data points are few and very scattered.

[27] Figure 10b shows wave orbital velocity skewness plotted against cross-shore migration velocity. In comparison to the mean cross-shore current, there is an association between cross-shore migration and skewness (R = 0.37). However, the observed skewnesses are uniformly positive and nonzero, while positive, negative and near-zero migration velocities were observed. This indicates that while wave orbital velocity skewness almost certainly played a role, it is unlikely that skewness alone can fully explain the observed migration velocities.

3.5. Megaripple Heights and Slopes

[28] Megaripple heights were obtained from the despiked, low-pass-filtered bed elevation profiles. Zero crossings of the first derivative of the bed elevation profile gave the positions of individual megaripple crests and troughs. Typically the heights were obtained as the difference between the highest and lowest points between two successive trough positions on the profiles.

[29] The resulting time series of megaripple height, η, are shown in Figure 11. Mean heights ranged from 0.05–0.5 m, which is consistent with the values observed by *Clifton et al.* [1971].

[30] The slopes of the steep shoreward faces were estimated from the bed elevation profiles in Figure 5. This segment of the data was particularly chosen because the megaripple relief in these profiles was clearly resolved and megaripples were unambiguously migrating onshore, in the direction of the steep faces. Only the segment between -2 m to $+1$ m horizontal distance was used. Beyond $+1$ m, steep shoreward advancing ripple faces were in acoustic shadow.
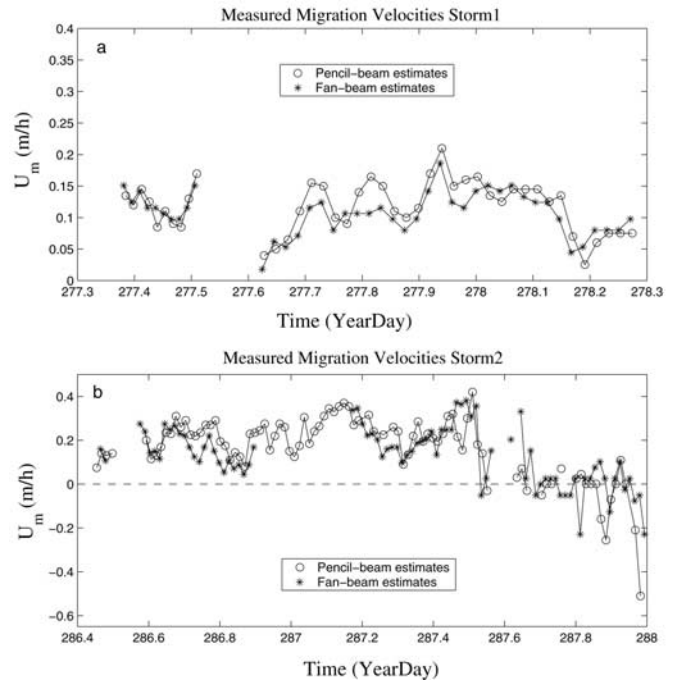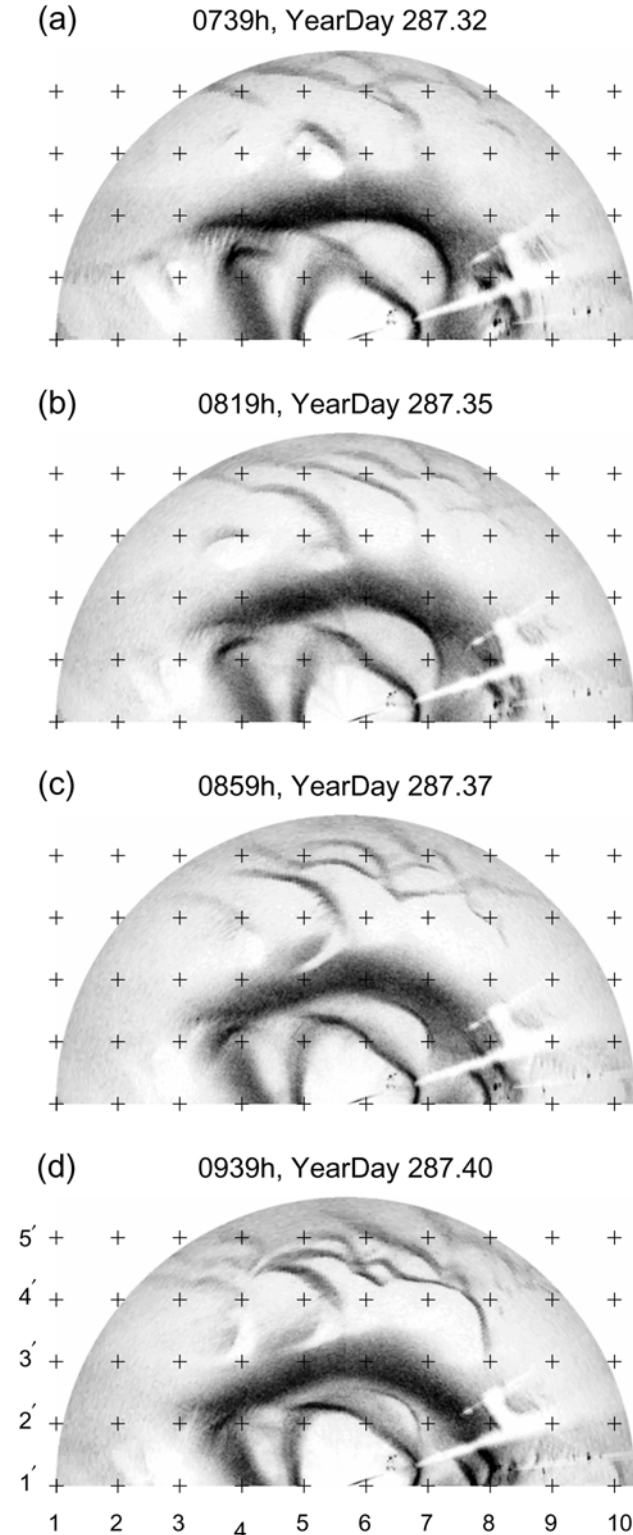
(a)   0739h, YearDay 287.32

(b)   0819h, YearDay 287.35

(c)   0859h, YearDay 287.37

(d)   0939h, YearDay 287.40

Figure 9. Measured cross-shore migration velocities (U_m) using pencil beam (circles) and fan beam (asterisks) data for (a) the Storm1 interval and (b) the Storm2 interval. Positive values indicate onshore migration. Note the general onshore migration, except late in the Storm2 interval.

Beyond -2 m, the resolution of bed profiles is too low for slope measurement.

[31] Figure 12 shows the histogram of the measured slopes. The distribution is rather broad, with a pronounced peak at $33°$, and no values greater than $37°$. The distribution is skewed toward low values, presumably because the pencil beam sometimes intersected megaripple profile along a line different from the line of maximum slope. Thus these results are consistent with the 28 to $36°$ angle of repose values suggested by *Cornforth* [1973] for saturated natural sandy sediments.

4. Theory

[32] *Bagnold* [1946] suggested a migration model for desert sand dunes in which dune advance occurs as a result

Figure 8. Fan beam images of lunate megaripples during the first stage of the Storm2 interval on the offshore side of the frame. The top of each image is offshore. Note the development of longshore (northward) oriented, nearly stationary, lunate features. Near grid point [5, 4′] in Figure 8a, for example, an initially irregular pit has developed in Figure 8c into a northward facing lunate megaripple: offshore horn tip onshore and north of grid point [5, 5′]; onshore horn tip near grid point [5, 3′]. The offshore limb is dark (high-amplitude backscatter from the steep slip face), and the onshore limb is light (steep face in acoustic shadow). By Figure 8d, this feature was more crescentic but, despite its orientation, had not migrated noticeably northward. Features farther offshore were migrating mainly onshore (e.g., near grid point [6, 5′]).
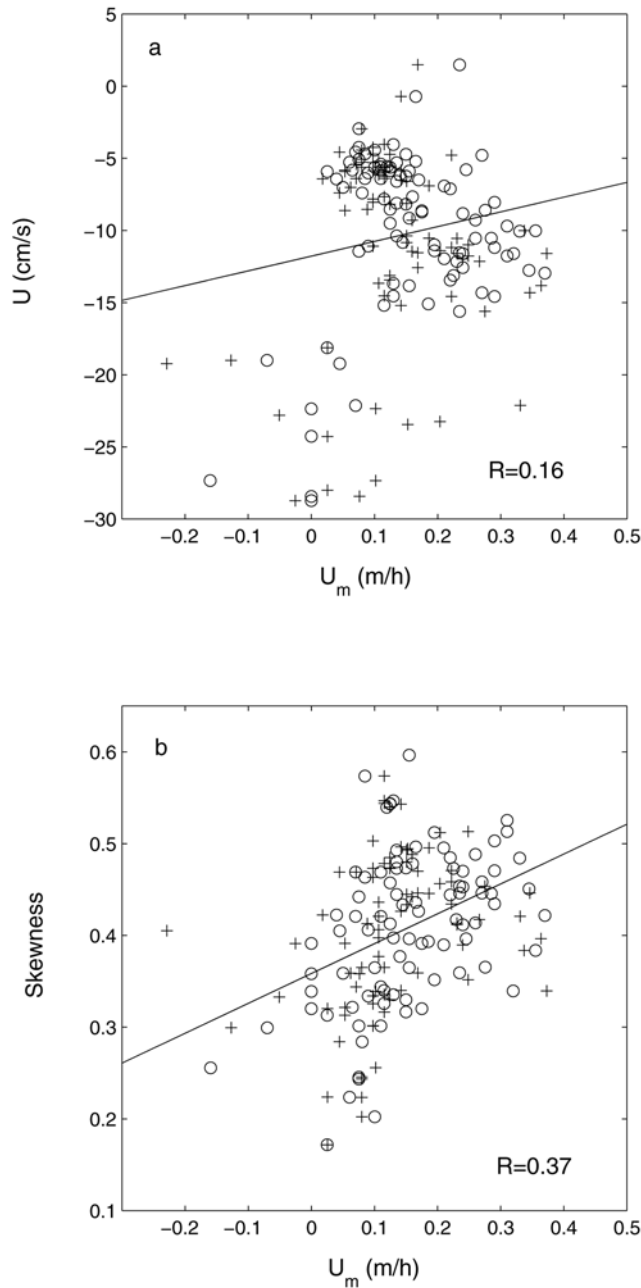
Figure 10. Comparisons between observed cross-shore migration velocities and (a) mean cross-shore velocity and (b) wave orbital velocity skewness for both the Storm1 and Storm2 intervals. Fan beam and pencil beam migration velocity estimates are represented by plus signs and open circles, respectively. The solid line is the best linear least squares fit; R is the correlation coefficient.

of sand avalanching down the steep front face of the dune, assumed to be at the angle of repose. In Bagnold's model, migration velocity U_m is related to the volumetric bed load transport rate per unit width Q_B and dune height η by

$$U_m = \frac{Q_B}{[\eta(1 - \epsilon)]} \qquad (1)$$

where ϵ is the sediment porosity. This model has been applied to unidirectional flows [see, e.g., *Middleton and Southard*,

1984, p. 279; *Fredsoe and Deigaard*, 1992, p. 266]. The present measurements indicate that megaripple heights were rather constant during the two storms (Figure 11), compared to the variations in migration rate (Figure 9). In particular, the slight trend toward decreasing ripple heights observed during both storms would, given equation (1) and assuming the other factors remained constant, indicate a trend toward increased migration speeds: such a trend was not observed. Thus the variability in the measured migration velocities cannot be attributed solely to changes in ripple height, and we therefore need to investigate the most likely alternative source of variation: the bed load transport.

[33] The cross-shore (x) component of the time-averaged bed load transport is given by

$$\overline{Q}_{Bx} = \hat{A}\overline{|\tau_b|^{\xi-1}\tau_{bx}} \qquad (2)$$

where $\hat{A}$ is an empirical constant, the overbar denotes an average over many wave cycles, τ_b is the bottom stress, and τ_{bx} its cross-shore component given by

$$\tau_{bx} = \tau_{cx} + \tau_{wx}, \qquad (3)$$

τ_{cx} and τ_{wx} being the cross-shore components of the current and wave stresses, respectively. The value of the stress exponent ξ in equation (2) is not well known [e.g., *Dyer and Soulsby*, 1988] but is often taken to be either 3/2 [*Meyer-Peter and Müller*, 1948] or 5/2 [*Sleath*, 1995].

[34] Following *Christoffersen and Johnsson* [1985] and *Sleath* [1995], the bed shear stress for combined waves and currents is given by a vector sum of the wave and current
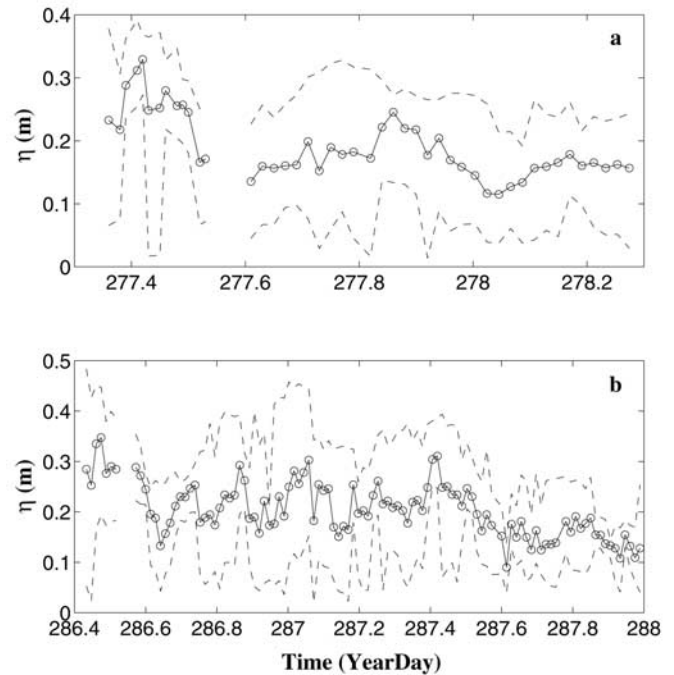

Figure 11. Measured megaripple heights (η) for (a) the Storm1 interval and (b) the Storm2 interval. The open circles connected by solid lines indicate mean values; the dashed lines indicate maximum and minimum values.
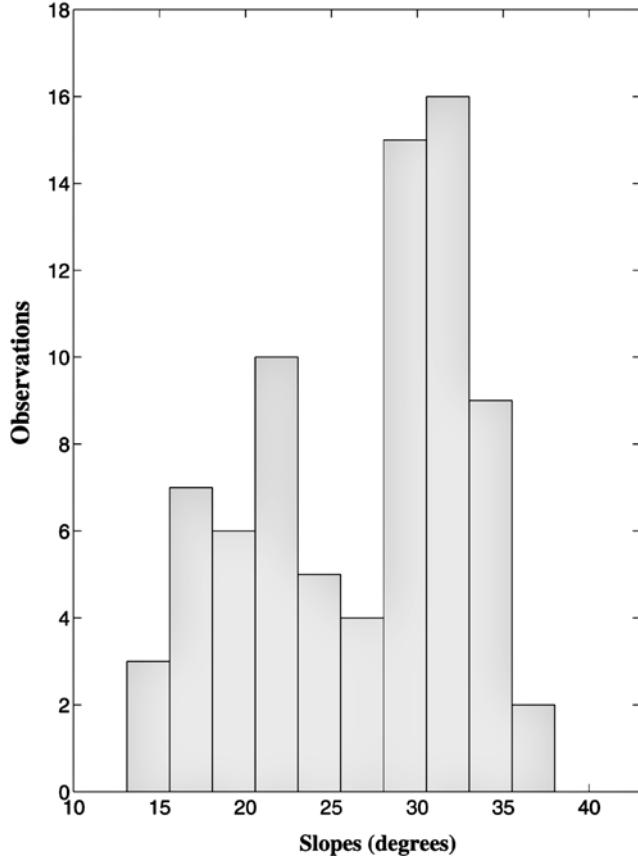
Figure 12. Histogram of slopes of the steep shoreward advancing megaripple faces determined from the bed elevation profiles shown in Figure 5, between −2 m and +1 m in cross-shore distance.

shear stresses: thus

$$\tau_b = \left[\tau_c^2 + \tau_w^2 + 2\left(\tau_{cx}\tau_{wx} + \tau_{cy}\tau_{wy}\right)\right]^{1/2}, \tag{4}$$

where

$$\tau_c = \left[\tau_{cx}^2 + \tau_{cy}^2\right]^{1/2} \tag{5}$$

and

$$\tau_w = \left[\tau_{wx}^2 + \tau_{wy}^2\right]^{1/2} \tag{6}$$

the subscripts x and y denoting the (x, y) components.

[35] The components of the mean current bed shear stress are

$$\left(\tau_{cx}, \tau_{cy}\right)/\rho = \frac{1}{2}f_c U_c(U, V) \tag{7}$$

where ρ is the water density, f_c the current friction factor, (U, V) the cross-shore and longshore currents respectively, and U_c is the magnitude of the current given by $U_c^2 = U^2 + V^2$.

[36] Similarly, the components of the wave bed shear stress are

$$\left(\tau_{wx}, \tau_{wy}\right)/\rho = \frac{1}{2}f_w U_{wo}(u_w, v_w), \tag{8}$$

where f_w is the wave friction factors, U_{wo} the wave orbital velocity amplitude, and (u_w, v_w) are the cross-shore and longshore components of the wave orbital velocity.

[37] Equations (7) and (8) were developed for mean currents and monochromatic waves. In nearshore field conditions, however, the waves are generally irregular and distributed over a range of frequencies in the incident (sea-and-swell) wave band. Significant energy is also often present in the infragravity frequency band between the zero frequency mean current and the sea-and-swell wave band. In order to investigate the relative importance of the different transport contributions by waves, mean currents and infragravity components, the instantaneous cross-shore (u) and alongshore (v) velocities were separated into three frequency bands such that

$$[u(t), v(t)] = \left[u_w(t) + U_{ig}(t) + U, \qquad v_w(t) + V_{ig}(t) + V\right], \tag{9}$$

where (U_{ig}, V_{ig}) represent the infragravity wave velocity components, and t is the time during each 1/2 hour data run. Estimating the relative contribution of the different bands to the stress raises the question of how best to specify the infragravity band friction factor, f_{ig}. Here, the calculations were performed for two cases: (1) the infragravity motions are treated as waves (U_{ig} and V_{ig} are added to u_w and v_w, and $f_{ig} = f_w$); and (2) the infragravity waves are considered to be current-like (U_{ig} and V_{ig} are added to U and V, and $f_{ig} = f_c$).

[38] Thus equation (2) can be rewritten as

$$\overline{Q_{Bx}} = \left[\hat{A}\left(\rho\sqrt{\alpha}f_c\right)^{\xi-1}\rho f_c\right]\overline{\chi(t, t_s)}, \tag{10}$$

where $\alpha = f_w/f_c$, t_s is a slow (wave-by-wave) timescale defined below, and χ is given by

$$\chi(t, t_s) = \frac{[Z(t, t_s)]^{\xi-1}}{2}\left\{U_c U + \alpha U_{wo}(t_s)u_w(t)\right\} \tag{11}$$

with

$$Z(t, t_s) = \left[\frac{U_c^4}{4\alpha} + \frac{\alpha U_{wo}(t_s)^2\left[u_w(t)^2 + v_w(t)^2\right]}{4}\right.$$
$$\left. + \frac{U_c U_{wo}(t_s)}{2}\left[Uu_w(t) + Vv_w(t)\right]\right]^{1/2}. \tag{12}$$

[39] In equation (11), the first term inside the curly brackets represents the cross-shore transport associated directly with the mean current, and the second term wave band transport. The infragravity band transport was included in one term or the other, as outlined above.

5. Modeling Cross-Shore Migration

[40] In order to calculate $\chi(t, t_s)$ in equation (11), a value is needed for α. The other velocity-based parameters are

readily obtained from the flowmeter records. As discussed in the next section, α was obtained by fitting the model-predicted $\overline{\chi}$ time series to the measured migration velocities. However, the approach used to estimate U_{wo} influences the resulting value of α. Two methods for determining U_{wo} were used, one much simpler to implement, but less consistent with the above equations.

5.1. Wave Orbital Velocity Amplitude

[41] The significant wave orbital velocity is given by $U_{wo} = 2\sqrt{U_{rms}^2 + v_{rms}^2}$ [*Thornton and Guza*, 1983]. This run-averaged wave orbital velocity statistic is referred to here as $2U_{rms}$. In this case U_{wo} is a constant for each 1/2 hour data run.

[42] A second approach is to calculate the orbital velocity amplitudes of individual waves from the peak crest and trough amplitudes for consecutive wave half cycles. This estimate is given by

$$U_{wo}(t_s) = \frac{A_{max1}(t_s) + A_{max2}(t_s)}{2}. \qquad (13)$$

where $A_{max1}(t_s)$ and $A_{max2}(t_s)$ respectively represent the maximum amplitudes in the $\sqrt{u_w^2 + v_w^2}$ time series during successive half cycles. The half-cycle time intervals were determined from the zero crossings in the u_w time series. Equation (13) is equivalent to half the peak-to-peak height and is thus designated the $0.5u_{pp}$ approach.

[43] The $0.5u_{pp}$ amplitudes vary on a wave-by-wave timescale t_s, slow compared to t, and defined for each data run as

$$t_{s(k)} = \sum_{n=1}^{k} (n-1)T_n + T_1/2 \qquad (14)$$

where k indicates the kth wave in the run, and T_n is the period of the nth wave.

[44] Both $2U_{rms}$ and $0.5u_{pp}$ include information on v_w, the longshore component of the wave orbital velocity. The $0.5u_{pp}(t_s)$ approach is likely to be more consistent with equation (10), as the time average of χ does not reduce in general to a dependence on the wave orbital velocity variance, at least not for half-integer values of ξ.

5.2. Friction Factors

[45] The wave and current friction factors are treated here as adjustable parameters, the values of which are products of the best fit between the modeled and measured migration rates. Comparisons are made later between the friction factors so obtained, and other estimates for combined wave-current flows over mobile beds under field conditions. As background for these comparisons, we summarize here the accepted relationships for wave and current friction factors over fixed beds.

[46] Following *Nielsen* [1992], the wave friction factor (in the absence of currents) for flat bed and fixed sand grain roughness is given by

$$\hat{f}_w = \exp\left[5.213\left(\frac{K_N}{A_{ws}}\right)^{0.194} - 5.977\right], \qquad (15)$$

where the carat denotes fixed roughness, A_{ws} is the significant wave orbital semiexcursion, and K_N is the Nikuradse sand roughness, taken to equal $2.5D_{50}$ where D_{50}

is the median grain diameter [*Jonsson*, 1966; *Nielsen*, 1992, p. 105]. Using Duck94 data values for significant wave orbital velocity of 65–90 cm/s, 6–8 s wave period, and 0.02 cm median grain diameter, equation (15) gives $\hat{f}_w$ in the range 8×10^{-3} to 9.5×10^{-3}.

[47] The current friction factor (in the absence of waves) for flat, immobile beds can be estimated using the Manning-Strickler formula [*Sleath*, 1984, p. 220]

$$\hat{f}_c = \frac{0.122}{4}\left(\frac{K_N}{h}\right)^{1/3}, \qquad (16)$$

where h is the water depth, and K_N is again taken to be $2.5D_{50}$. For 3 m water depth, equation (16) gives $\hat{f}_c = 1.7 \times 10^{-3}$.

[48] Thus the fixed grain roughness value of $\alpha = f_w/f_c$, estimated from wave-only f_w and current-only f_c values, would be O(10). However, for combined flows the friction coefficients are different, and in particular f_c is expected to increase because of increased turbulent momentum flux in the wave bottom boundary layer. Therefore, one might expect that α would be reduced. However, the above estimates are for fixed grain flat bed roughness, whereas we are dealing with a mobile bed, for which the effective roughness of the bed for both current and waves may be quite different because of active adjustment of the bed itself.

[49] Now, noting that χ depends on α but not f_c (equation (11)), best fit values of α can be estimated by computing the correlation between the observed migration velocity time series and the model-predicted time series of $\overline{\chi}$, using equation (11) to compute $\chi(t, t_s)$ for each run and then averaging over the run. Figure 13 shows the correlation coefficients between $\overline{\chi}$ and the measured migration velocities as a function of α, for the different values of ξ, the two U_{wo} estimators, and the wave-like and current-like treatments of the infragravity band. Note that the correlation peaks are much more distinct for the $0.5u_{pp}$ approach for estimating wave orbital velocity amplitude, compared to the $2U_{rms}$ method. Table 1 summarizes the results in Figure 13, listing the peak correlation coefficients, R, and the corresponding values of α. The values of R range from 0.61–0.65 for all cases considered: this represents a significant improvement over the correlation coefficients between migration velocity and cross-shore current (0.16) or wave orbital velocity skewness (0.37; see Figure 10).

[50] Figure 14 shows the predicted $\overline{\chi}$ time series for the Storm2 interval (computed using the values of α in Table 2) separated into the contributions from the sea-and-swell and infragravity wave bands, and from the mean current, for $\xi = 3/2$. The predicted sea-and-swell contribution is positive (onshore), for both the current-like (Figure 14a) and the wave-like (Figure 14b) treatments of $U_{ig}(t)$ and $V_{ig}(t)$. In contrast, the predicted infragravity band and mean contributions are persistently negative (offshore) for both cases. Note also that for the wave-like treatment of the infragravity band, its contribution is predicted to have been comparable to the mean current contribution for much of the record (whereas the current-like treatment leads to a considerably smaller contribution).

5.3. Model Results

[51] As by *Sleath* [1995], the time-averaged bed load transport rate in equation (2) can be written in nondimensional form by dividing the left-hand side by $[(s-1)gD^3]^{1/2}$,
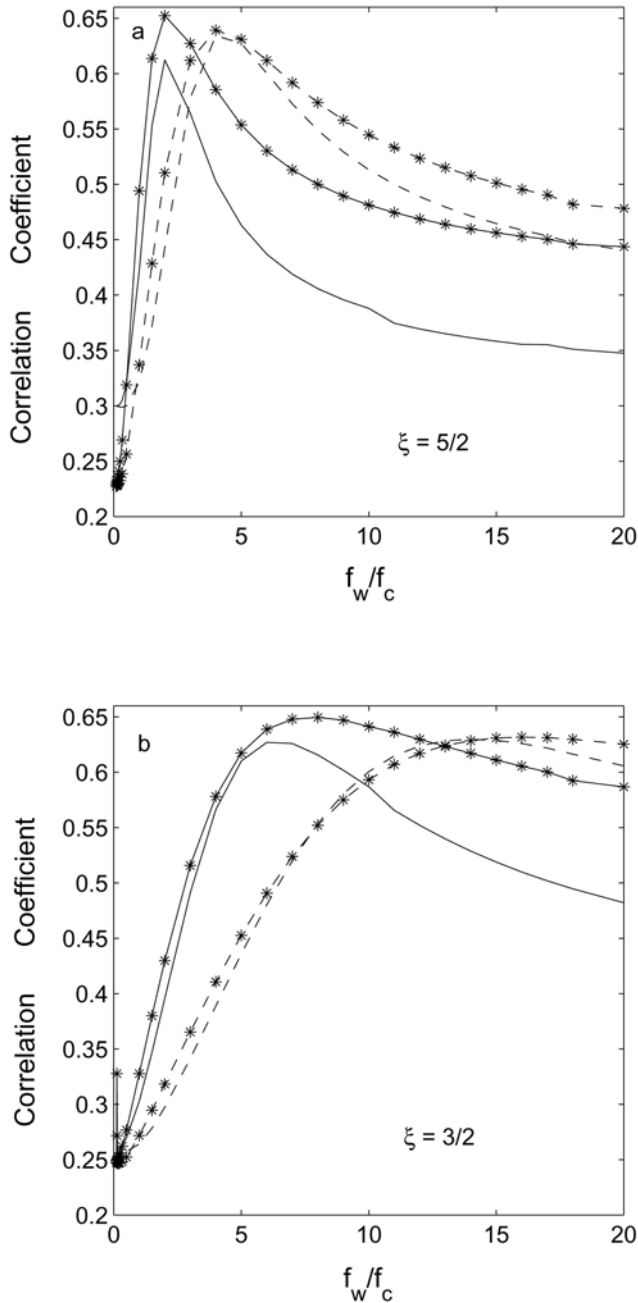
Figure 13. Correlation coefficients between measured migration velocities and $\overline{\chi}$ for both the Storm1 and Storm2 intervals as a function of friction coefficient ratio, $\alpha = f_w/f_c$. The solid lines are the results for $U_{wo}(t_s) = 0.5u_{pp}(t)$; the dashed lines are for $U_{wo} = 2U_{rms}$. Asterisks are for the case with infragravity velocities treated as waves; lines with no symbols are for infragravity velocities treated as currents.

where s is the specific gravity of the sediment grains, and the right-hand side by $[\rho(s-1)gD]^{\xi}$. Thus the nondimensional cross-shore time-averaged bed load transport rate is, from equation (10),

$$\overline{\Phi}_{Bx} = \frac{\overline{Q}_{Bx}}{[(s-1)gD^3]^{1/2}} = \frac{A(\rho\sqrt{\alpha}f_c)^{\xi-1}\rho f_c}{[\rho(s-1)gD]^{\xi}}\overline{\chi(t,t_s)},$$

giving

$$\overline{Q}_{Bx} = \frac{A(\sqrt{\alpha}f_c)^{\xi-1}f_cD}{[(s-1)gD]^{\xi-1/2}}\overline{\chi(t,t_s)}. \tag{17}$$

Combining equation (1) and equation (17), the predicted migration velocity is

$$U_m = A\left[\frac{D(\sqrt{\alpha})^{\xi-1}f_c^{\xi}}{\eta(1-\epsilon)[(s-1)gD]^{\xi-1/2}}\right]\overline{\chi(t,t_s)}. \tag{18}$$

Model parameters are sediment specific gravity $s = 2.7$; grain diameter $D = D_{50}$, 0.02 cm; sediment porosity $\epsilon = 0.4$. For $\xi = 5/2$, the value of the empirical constant A was set to 0.4, the rough bed value given by *Sleath* [1995]. For $\xi = 3/2$, $A = 8$ was chosen, following *Meyer-Peter and Müller* [1948]. The velocity time series were from the lower flowmeter on the seaward side of the frame; the η time series the measured means (open circles in Figure 11).

[52] Figure 15 shows an example comparison between modeled and measured cross-shore migration velocity time series for the Storm2 interval using the $0.5u_{pp}$ approach. The directions and magnitudes of measured megaripple migration velocities both agree reasonably well with those predicted by the model. Given that there are only two fitted parameters in the model, f_c and α, the values of which are held constant (i.e., independent of time), it is encouraging that the time dependence of the predicted and observed migration velocities are qualitatively similar: in particular, the observed tendencies for migration first to stall and then trend offshore at the end of the Storm2 interval are reproduced in the model results. Other low-frequency variations in the observed time series are also predicted: in particular, the approximately 12 hour period oscillation, reflecting the modulation of the wave forcing by sealevel changes associated with the semidiurnal tide. There are also, however, features in the observations which are not well predicted: the observed amplitude of the semidiurnal variation is less (about half) of that predicted, and there is an observed trend toward increased onshore migration before YD287.5 which is not present in the predictions.

[53] The predicted migration velocities were linearly regressed against the observations to obtain correlation coefficients (R) and the slopes (S) of the best fit regression

Table 1. Maximum Correlation Coefficients (R) Between Measured Megaripple Migration Velocities and $\overline{\chi}$ and the Corresponding Value of $\alpha = f_w/f_c$ (see Figure 13) for Both the RMS and Peak-to-Peak Methods for Estimating U_{wo}, Both Wave-Like and Current-Like Treatments of the Infragravity Band, and Both 3/2 and 5/2 Values for the Stress Exponent ξ

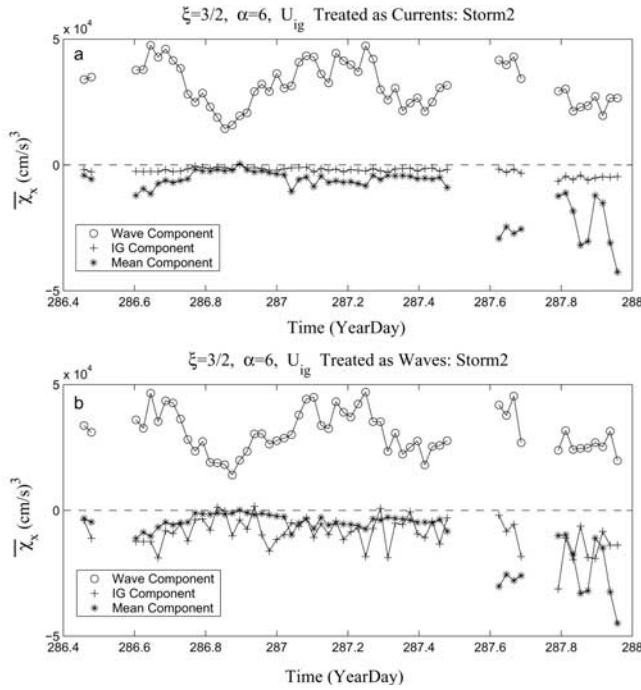| U_{wo}	U_{ig}, V_{ig}	ξ	α	R
$0.5u_{pp}(t_s)$	as waves	3/2	8	0.65
$0.5u_{pp}(t_s)$	as currents	3/2	6	0.63
$0.5u_{pp}(t_s)$	as waves	5/2	2	0.65
$0.5u_{pp}(t_s)$	as currents	5/2	2	0.61
$2U_{rms}$	as waves	3/2	16	0.63
$2U_{rms}$	as currents	3/2	14	0.63
$2U_{rms}$	as waves	5/2	4	0.64
$2U_{rms}$	as currents	5/2	4	0.63

Figure 14. Wave, infragravity and mean components of $\overline{\chi}$ for the Storm2 interval, computed with $\xi = 3/2$ using the wave-by-wave $u_{pp}(t_s)$ method for computing U_{wo} and (a) the current-like and (b) the wave-like treatments of the infragravity band.

line. Scatterplots of the predicted and observed migration velocities are shown in Figure 16, together with the regression lines, for U_{wo} determined using $0.5u_{pp}(t_s)$, both the wave-like current-like treatments of the infragravity band, and the two values of ξ. The values of R and S are listed in Table 2. The correlation coefficients are all quite similar, between 0.53 and 0.59. The slopes, however, are closer to unity for the wave-like treatment of the infragravity band, and closest to unity for $\xi = 3/2$ using the wave-by-wave ($0.5u_{pp}(t_s)$) determination of U_{wo}.

[54] To reduce the effects of noise in the data, the measured migration velocities were divided into six equal (0.1 m/h) nonoverlapping intervals. The average measured and predicted migration rates (these averages being computed from the points within each interval) are plotted in Figure 17. The dashed lines indicate the 1:1 relation, solid

lines the regression line. The values of R_I and S_I, the correlation coefficient and slope of the regression line, are listed in Table 2. The correlation coefficients R_I are all above 0.9, considerably higher than the correlation coefficients obtained using the unaveraged results, reflecting the smaller number of points but consistent with a linear relationship between prediction and measurement.

[55] The final column in Table 2 is the wave friction factor, f_w, computed from α and f_c, but only for those rows with slopes S_I and S closest to unity compared to the adjacent row with the same value of ξ. It can be seen that, in all cases but one, these rows correspond to the wave-like treatment of the infragravity band. Furthermore, for each pair of rows with an f_w value and the same ξ value, the slopes are closer to unity for the wave-by-wave ($0.5u_{pp}$) computation of U_{wo}.

6. Discussion

[56] The best fit values of f_w in Table 2 are 0.017 for $\xi = 5/2$, and 0.048 for $\xi = 3/2$: 2 to 5 times larger than the flat bed, fixed bottom roughness, wave-only values obtained for $\hat{f}_w$ from equation (15). Estimates by *Smyth and Hay* [2002] of the wave friction factor for mobile sandy sediments in the nearshore zone, based on near-bed turbulence intensity and the vertically integrated horizontal momentum deficit equation, indicate that f_w would be expected to range from 0.02 to 0.01 for $0.6 < \theta_{2.5} < 1$, in agreement with the predictions of *Tolman*'s [1994] semiempirical formulation. $\theta_{2.5}$ is the grain roughness Shields parameter [*Nielsen*, 1992]:

$$\theta_{2.5} = \tau_{wo}/[(s-1)\rho g 2.5 D_{50}] \qquad (19)$$

where τ_{wo} is the maximum stress in a half wave cycle or, from equation (8), $\rho f_w U_{wo}^2/2$. For the present data set, on the basis of significant wave orbital velocity, $\theta_{2.5}$ ranged from 0.6 to 1.4 for the Storm1 and Storm2 intervals combined [*Ngusaru*, 2000, p. 94]. The Smyth and Hay f_w estimates were obtained for values of the Shields parameter less than unity. Furthermore, at $\theta_{2.5} \sim O(1)$ in their data, the bed was flat. The lunate megaripples at higher Shields parameters in the present data set indicate a different (and higher) bottom roughness regime, outside the range of the Smyth and Hay observations. The 0.01 to 0.02 range should therefore be regarded as a reasonable lower bound on f_w and, as such, consistent with the range of values 0.017 to 0.048 given above.

Table 2. Results of Linearly Regressing Computed Against Measured Cross-Shore Migration Velocities[a]

U_{wo}	U_{ig}, V_{ig}	ξ	α	f_c	R	S	R_I	S_I	f_w
$0.5u_{pp}(t_s)$	as waves	3/2	6	8.0×10^{-3}	0.59	0.84	0.93	0.68	0.048
$0.5u_{pp}(t_s)$	as currents	3/2	6	8.0×10^{-3}	0.53	0.69	0.94	0.43	
$0.5u_{pp}(t_s)$	as waves	5/2	2	4.5×10^{-3}	0.59	0.98	0.95	0.68	0.009
$0.5u_{pp}(t_s)$	as currents	5/2	2	4.5×10^{-3}	0.54	0.86	0.94	0.56	
$2U_{rms}$	as waves	3/2	15	6.0×10^{-3}	0.54	0.68	0.93	0.47	
$2U_{rms}$	as currents	3/2	15	6.0×10^{-3}	0.53	0.67	0.95	0.48	0.090
$2U_{rms}$	as waves	5/2	4	4.3×10^{-3}	0.57	0.94	0.94	0.65	0.017
$2U_{rms}$	as currents	5/2	4	4.3×10^{-3}	0.57	0.82	0.97	0.63	

[a]R and S are the correlation coefficients and slopes of linear regression lines using the results from all data runs individually; R_I and S_I are the from the regression lines based on the interval-averaged data in Figure 16. The values of $\alpha = f_w/f_c$ and f_c used in the model calculations are shown and were based on Table 1. Also shown explicitly are the values of f_w, based on α and f_c, for the best overall fits (highest correlations, slopes nearest unity) for both U_{wo} estimators and both values of ξ.

[57] The values of f_c corresponding to the above best fit values of f_w are 4.3×10^{-3} and 8.0×10^{-3}, for $\xi = 5/2$ and $3/2$ respectively (Table 2). These f_c values are 2.5 to 5 times higher than the flat bed, fixed roughness, current-only $\hat{f}_c$ value, computed using equation (16). Higher values of f_c are expected in the presence of high-amplitude, steep bed forms, and the additional vertical momentum flux arising, in combined flows, from wave-generated turbulence.

[58] Since the bottom drag coefficient $C_d = f_c/2$, the corresponding values of C_d are 2.1×10^{-3} and 4.0×10^{-3}. Note that given the definition of f_c in equation (5), these values of C_d would apply equally to the cross- and along-shore components of the mean current. Values of C_d were determined during Duck94 by *Garcez Faria et al.* [1998] from vertical profiles of the longshore current: specifically, using the law-of-the-wall

$$V(z) = \frac{v_*}{\kappa} \ln\left(\frac{z+h}{z_a}\right) \tag{20}$$

where κ is von Karman's constant and z_a is the apparent bottom roughness felt by the longshore current in the
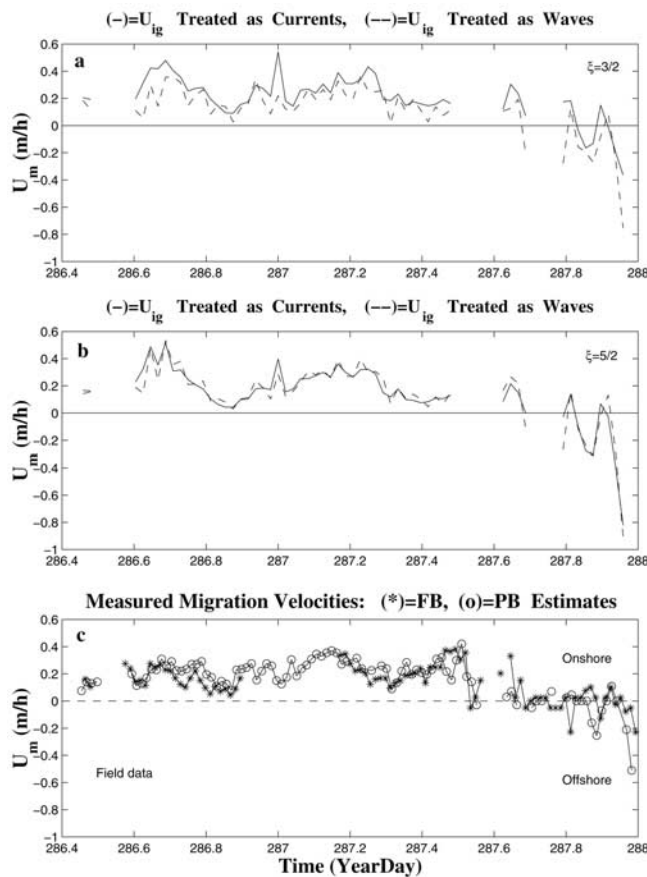

Figure 15. Modeled and measured cross-shore megaripple migration velocities for the Storm2 interval. The model predictions, shown in Figures 15a and 15b are for $U_{wo} = 0.5u_{pp}(t_s)$ with $U_{ig}(t)$ and $V_{ig}(t)$ treated as waves (dashed) or as currents (solid): (a) $\xi = 3/2$ and (b) $\xi = 5/2$. (c) The observations show the migration velocities determined from the fan beam (asterisks) and the pencil beam (open circles).
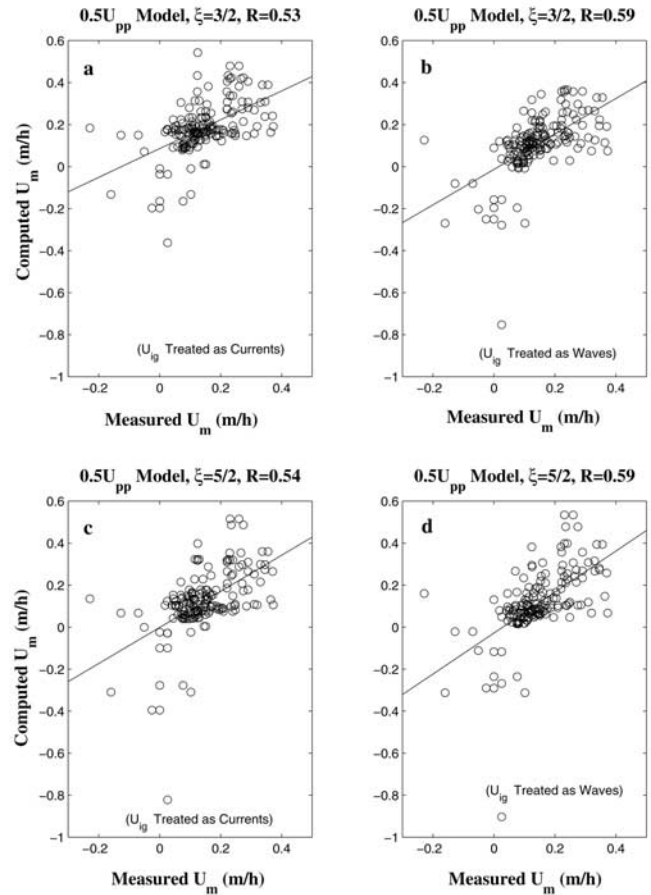

Figure 16. Comparisons between measured and computed cross-shore migration velocities using the $U_{wo} = 0.5u_{pp}(t_s)$ with (a) U_{ig} and V_{ig} treated as currents and $\xi = 3/2$, (b) U_{ig} and V_{ig} treated as waves and $\xi = 3/2$, (c) U_{ig} and V_{ig} treated as currents and $\xi = 5/2$, and (d) U_{ig} and V_{ig} treated as waves and $\xi = 5/2$. The linear regression lines (solid) are shown. R is the correlation coefficient. See also Table 2.

presence of waves. *Garcez Faria et al.* [1998] defined C_d as the ratio of v_*^2 to a mean square velocity which included the turbulent and wave velocities in addition to the mean current. This is different from the definition of $f_c/2$ used here, which is based on the mean current alone (equation (7)). However, the values of v_* given by Garcez Faria et al. can be used together with their measurements of V, and τ_{cy} as represented in equation (8), to obtain C_d estimates consistent with the definition used here. Garcez Faria et al. also estimated v_{*s}, the component of the bed friction velocity due solely to shear stress at the bed (i.e., not including the form drag produced by the bed forms): it is this part of the turbulent stress which directly forces sediment transport, and which is represented in the theory used here. Specifically then, using v_{*s} as reported by Garcez Faria et al. for 10, 11, and 12 October (year days 283 to 285) at cross-shore distances of 185, 187 and 188 m (the locations nearest our frame), and V at 1 m height determined from their plotted profiles (65, 60, and 50 cm/s), we obtain values of C_d equal to 3.6×10^{-3}, 1.6×10^{-3}, and 1.9×10^{-3}. These values are in close agreement with the $f_c/2$ values given above (2.1×10^{-3} and 4.0×10^{-3}).
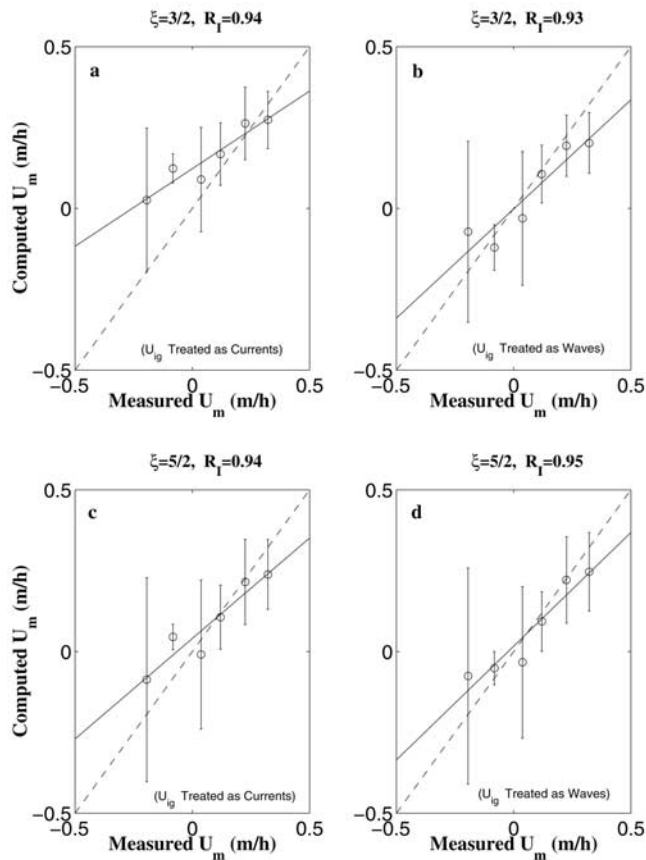
Figure 17. Comparisons between interval-averaged measured and computed cross-shore migration velocities using $U_{wo} = 0.5u_{pp}(t_s)$ with (a) U_{ig} and V_{ig} treated as currents and $\xi = 3/2$, (b) U_{ig} and V_{ig} treated as waves and $\xi = 3/2$, (c) U_{ig} and V_{ig} treated as currents and $\xi = 5/2$, and (d) U_{ig} and V_{ig} treated as waves and $\xi = 5/2$. The linear regression lines (solid) and 1:1 lines (dashed) are shown. R_I is the correlation coefficient. Vertical bars denote ±1 standard deviation within each interval (number of points per 0.1 m/h interval, from left to right: 2, 3, 26, 88, 35, and 18).

[59] Another independent value for f_c can be obtained from the Manning-Strickler formula, using the bed form roughness instead of the grain roughness. Thus, setting K_N equal to the RMS bed elevation and taking the latter to be $\sim \eta/2^{3/2}$ with $\eta = 20$ cm (Figure 11), equation (16) gives $f_c = 8.7 \times 10^{-3}$. This estimate is a factor of 2 to 4 greater than the measured values and, since it includes form drag, should be regarded as an upper bound.

[60] Thus, while much remains to be learned about bottom stress and friction coefficients in turbulent combined wave-current flows over mobile beds, the values of f_w and f_c obtained here are not outside the ranges expected. That is, the wave friction factors are several times larger than the fixed grain, flat bed, wave-only values, and somewhat larger than the mobile grain, flat bed results obtained by Smyth and Hay. The current friction factors f_c are (1) also several times larger than the fixed grain, flat bed, current-only value; (2) comparable to the values obtained from bed shear stress estimates made independently by Garcez Faria et al. during same experiment at comparable positions offshore;

and (3) less than the value obtained using the rms bed elevation for the bed roughness in the Manning-Strickler formula which includes form drag.

[61] Note also that the values of the friction coefficients obtained from the ripple migration rates are strongly dependent upon the value assumed for the stress exponent in the bed load transport model. Furthermore, this dependence is such that lower friction factors correspond to higher values of ξ.

[62] Finally, recall that the velocities used in the migration model were those measured by the lower flowmeter on the seaward side of the frame. The question arises as to the possible effects of the flowmeter height on the results. Sensor height is unlikely to have significantly affected the wave orbital velocities, as 6–9 s period waves are essentially shallow water in 2 m water depth. The effect on the longshore current V can be estimated from the law of the wall, giving an increase $2.6v_*$ if the measurements at 35 cm height were adjusted to 1 m. Using Garcez Faria et al.'s values for v_* including form drag (7.0, 5.2, and 4.7 cm/s), reduced by the ratio of our measured longshore current speed to their values of V at 1 m height given above, would raise our values of V by only about 25%: specifically, 20 cm/s longshore current speed at 35 cm height would increase by 4.5 to 5.6 cm/s. The vertical shear of the cross-shore mean flow is not governed by a law-of-the-wall relationship, however, but by the undertow dynamics [*Haines and Sallenger*, 1994; *Garcez Faria et al.*, 2000]. Correcting the measured mean currents to 1 m height could in fact produce lower current speeds, as the vertical shear of the mean cross-shore current is negative over much of the water column. Attempting to correct the mean cross-shore current to 1 m height is clearly not appropriate: it is not in fact clear what an appropriate height would be. We have elected to use the sensor height which, on the basis of the cross-shore current profiles obtained during Duck94 by *Garcez Faria et al.* [2000], should have been near the level of maximum offshore flow. Irrespective of either the relatively small increase in V from an adjustment to 1 m height, or the lack of an obvious reference height to choose for U, it is unlikely that the friction factors resulting from the fit to the migration model would be as sensitive to the choice of reference level for the mean current as they are to the value of ξ.

7. Conclusions

[63] Using plan view images and cross-shore bed elevation profiles obtained with rotary acoustic sounders during two storm events when longshore currents were weak, meter-scale lunate megaripples have been shown to migrate onshore with horns directed shoreward at speeds of 10–40 cm/h, against the 5–20 cm/s offshore current. The slopes of the shoreward advancing megaripple faces were 30–33°, close to the angle of repose, consistent with the avalanche mechanism of bed form migration. At large (>20 cm/s) offshore current speeds, migration stalled and appears to have shifted to the offshore direction at the end of the data record. This period was however also characterized by 20–50 cm/s northward mean longshore currents, resulting in the development of northward oriented megaripples: thus the apparent offshore migration occurred in association with

growth of northward facing lunate forms, and northward rotation of initially onshore facing megaripples.

[64] Cross-shore migration velocities predicted using a stress-based bed load sediment transport model combined with the *Bagnold* [1946] dune migration model are reasonably consistent with the measured migration velocities. The predictions depend upon only two fitted parameters: the wave and current friction factors f_w and f_c. The best fit values of these parameters are well within the range expected on the basis of available field and laboratory measurements (see Discussion). Thus, given that the predicted migration velocity time series were computed using constant friction factors (i.e., independent of time and the same values for both storm periods) and given as well the lack of consensus as to the governing equations for sediment transport in combined flows, the agreement between predicted migration rates both quantitatively (magnitude and sign) and qualitatively (variation through time) might even be considered remarkable. However, neither the amplitude of semidiurnal frequency variations in the observed migration velocities nor the low-frequency trend are well predicted, and the correlation between predicted and observed migration velocities is only ~0.6. A major factor contributing to the low correlations is undoubtedly the noisiness in the observed time series: the observed migration speeds themselves, and the megaripple heights. The low correlations may also indicate something missing from the model. One definite question mark in that regard is the essentially 2-D nature of Bagnold's model and the clear three-dimensionality of the megaripple fields observed in this study. These are questions to be explored in future investigations.

[65] In the analysis, the velocity spectrum was partitioned into zero (mean current), infragravity, and sea-and-swell frequency bands. The infragravity band was treated as either wave-like or current-like: the wave-like treatment yielded better agreement between measured and predicted migration velocities. The velocity amplitude of the incident sea-and-swell band, which appears in the theory through the wave-induced bed shear stress, was determined in two ways: one based on the velocity variance for each data run; the other determined wave by wave during each run from a zero-crossing analysis of the velocity time series. The migration velocity predictions made using the wave-by-wave determination of wave amplitude are in better agreement with the observations.

[66] In the theory, two values were used for the bottom shear stress exponent ξ: 3/2 and 5/2. The choice between the two values of ξ made little difference to the agreement between predicted and observed migration rates. In contrast, the best fit values for the friction factors were found to be strongly dependent upon the stress exponent, f_w increasing by a factor of 5 and f_c by a factor of 2, when ξ was reduced from 5/2 to 3/2.

References

Allen, J. R. L. (1968), *Current Ripples: Their Relation to Patterns of Water and Sedimenation Motion*, 433 pp., North-Holland, New York.

Bagnold, R. A. (1946), *The Physics of Blown Sand and Desert Dunes*, 265 pp., Chapman and Hall, New York.

Birkemeier, W. A., H. C. Miller, S. D. Wilheim, A. E. DeWall, and C. S. Gorbics (1985), A user's guide to the Coastal Engineering Research Center's (CERC's) Field Research Facility, *Instr. Rep. CERC-85-1*, 136 pp., Waterw. Exp. Stn., Corps of Eng., Vicksburg, Miss.

Boyd, R., D. L. Forbes, and D. E. Heffler (1988), Time-sequence observations of wave-formed sand ripples on an ocean shoreface, *Sedimentology*, *35*, 449–464.

Christoffersen, J. B., and I. V. Johnsson (1985), Bed friction and dissipation in a combined current and wave motion, *Ocean Eng.*, *12*, 387–423.

Clifton, H. E., R. E. Hunter, and R. L. Phillips (1971), Depositional structures and processes in the non-barred high-energy nearshore, *J. Sediment. Petrol.*, *41*, 651–670.

Cornforth, D. H. (1973), Prediction of drained strength of sands from relative density measurements, *ASTM Spec. Tech. Publ.*, *523*, 281–303.

Crawford, A. M., and A. E. Hay (1998), A simple system for laser-Illuminated video imaging of sediment suspension and bed topography, *IEEE J. Oceanic. Eng.*, *23*, 12–19.

Davidson-Arnott, R. G. D., and B. Greenwood (1976), Facies relationships on a barred coast, Kouchibouguac Bay, New Brunswick, Canada, in *Beach and Nearshore Sedimentation*, edited by R. A. Davis Jr. and R. L. Ethington, *Spec. Publ. Soc. Econ. Paleontol. Mineral.*, *24*, 149–168.

Dingler, J. R. (1974), Wave-formed ripples in nearshore sands, Ph.D. diss., 136 pp., Univ. of Calif., San Diego.

Dingler, J. R., J. C. Boylls, and R. L. Lowe (1977), A high-frequency sonar for profiling small-scale subaqueous bedforms, *Mar. Geol*, *24*, 279–288.

Dyer, K. R., and R. L. Soulsby (1988), Sand transport on the continental shelf, *Annu. Rev. Fluid Mech.*, *20*, 295–324.

Fredsoe, J., and R. Deigaard (1992), *Mechanics of Coastal Sediment Transport*, 369 pp., World Sci., River Edge, N. J.

Gallagher, E. L., S. Elgar, and E. D. Thornton (1998), Observations and predictions of megaripple migration in a natural surf-zone, *Nature*, *394*, 165–168.

Garcez Faria, A. F., E. B. Thornton, T. P. Stanton, and C. V. Soares (1998), Vertical profiles of longshore currents and relates bed shear stress and bottom roughness, *J. Geophys. Res.*, *103*, 3217–3232.

Garcez Faria, A. F., E. B. Thornton, T. C. Lippmann, and T. P. Stanton (2000), Undertow over a barred beach, *J. Geophys. Res.*, *105*, 16,999–17,010.

Grant, W. D., and O. S. Madsen (1986), The continental shelf bottom boundary layer, *Annu. Rev. Fluid Mech.*, *18*, 265–305.

Haines, J. W., and A. H. Sallenger Jr. (1994), Vertical structure of mean cross-shore currents across a barred surf zone, *J. Geophys. Res.*, *99*, 14,223–14,242.

Hay, A. E., and A. J. Bowen (1993), Spatially correlated depth changes in the nearshore zone during autumn storms, *J. Geophys. Res.*, *98*, 12,387–12,404.

Hay, A. E., and D. L. Wilson (1994), Rotary sidescan images of nearshore bedform evolution during a storm, *Mar. Geol.*, *119*, 57–65.

Jonsson, I. G. (1966), Wave boundary layers and friction factors, paper presented at 10th Coastal Engineering Conference, Am. Soc. of Civ. Eng., Tokyo.

Kachel, N. B., and R. W. Sternberg (1971), Transport of bedload as ripples during an ebb current, *Mar. Geol.*, *10*, 229–244.

Meyer-Peter, E., and R. Müller (1948), Formula for bed-load transport, paper presented at 2nd Meeting of the International Association for Hydraulic Structural Research, Stockholm.

Middleton, G. V., and J. B. Southard (1984), *Mechanics of Sediment Movement*, Soc. for Sediment. Geol., Tulsa, Okla.

Ngusaru, A. S. (2000), Cross-shore migration of lunate megaripples and bedload sediment transport models, Ph.D. thesis, 193 pp., Mem. Univ. of Newfoundland, St. John's, Newfoundland, Canada.

Nielsen, P. (1992), *Coastal Bottom Boundary Layers and Sediment Transport*, 324 pp., World Sci., River Edge, N. J.

Osborne, P. D., and C. E. Vincent (1992), Timescales of bed response in a low energy surf zone, paper presented at 23th Coastal Engineering Conference, Am. Soc. of Civ. Eng., Venice, Italy.

Sleath, J. F. A. (1984), *Sea Bed Mechanics*, 335 pp., John Wiley, New York.

Sleath, J. F. A. (1995), Sediment transport by waves and currents, *J. Geophy. Res.*, *100*, 10,977–10,986.

Smyth, C., and A. E. Hay (2002), Wave friction factors in nearshore sands, *J. Phys. Oceanogr.*, *32*, 3490–3498.

Thornton, E. B., and R. T. Guza (1983), Transformation of wave height distribution, *J. Geophys. Res.*, *88*, 5925–5938.

Tolman, H. L. (1994), Wind waves and movable-bed bottom friction, *J. Phys. Oceanogr.*, *24*, 994–1009.

Traykovski, P., A. E. Hay, J. D. Irish, and J. F. Lynch (1999), Geometry, migration, and evolution of wave orbital ripples at LEO-15, *J. Geophys. Res.*, *104*, 1505–1524.

Vincent, C. E., and P. D. Osborne (1993), bedform dimensions and migration rates under shoaling and breaking waves, *Cont. Shelf Res.*, *13*, 1267–1280.

Wright, L. D., J. D. Boon, and J. J. List (1991), Modes of cross-shore sediment transport on the shoreface of the middle Atlantic bight, *Mar. Geol.*, *96*, 19–51.

—————————

A. E. Hay, Department of Oceanography, Dalhousie University, Halifax, Nova Scotia, Canada, B3H 4J1. (alex.hay@dal.ca)

A. S. Ngusaru, Institute of Marine Sciences, University of Dar es Salaam, P.O. Box 668, Zanzibar, Tanzania. (angusaru@zims.udsm.ac.tz)